Journal of Luminescence 224 (2020) 117273

Contents lists available at ScienceDirect

Journal of Luminescence

journal homepage: http://www.elsevier.com/locate/jlumin

Structural and optical properties of ZnO–Al_2O_3 nanopowders prepared by chemical methods

N. Romcevic [a], B. Hadzic [a,*], M. Romcevic [a], N. Paunovic [a], D. Sibera [b], U. Narkiewicz [b], I. Kuryliszyn-Kudelska [c], J.L. Ristic-Djurovic [a], W.D. Dobrowolski [c]

[a] Institute of Physics, University of Belgrade, Pregrevica 118, 11080, Belgrade, Serbia
[b] West Pomeranian University of Technology, Institute of Chemical and Environment Engineering, Pulaskiego 10, 70-322, Szczecin, Poland
[c] Institute of Physics, Polish Academy of Science, Aleja Lotnikow 32/46, PL-02668, Warszawa, Poland

ARTICLE INFO

Keywords:
Semiconductors
Optical properties
Photoluminescence
Infrared spectroscopy
Nanostructures

ABSTRACT

The nanopowders of $(ZnO)_{1-x}(Al2O3)_x$, where x ranges from 0 to 0.7, were obtained by two chemical methods: the co-precipitation/calcination and hydrothermal synthesis. The first assessment of structural and optical properties of the obtained nanopowders was undertaken by the SEM, XRD, Raman and far-infrared spectroscopy, which was followed by the photoluminescence spectroscopy at room temperature. The obtained far-infrared reflectivity spectra were analyzed using the fitting procedure. The dielectric function of ZnO–Al_2O_3 nanopowders was modeled by the Maxwell-Garnet formula under the assumption that the nanopowders are a mixture of homogenous spherical inclusions in air. The combined plasmon-LO phonon modes (CPPM) were observed in the far-infrared reflection spectra. The photoluminescence spectra contain emissions related to the presence of ZnO, $ZnAl_2O_4$, and AlOOH phases in the nanomaterial, which is in agreement with the results obtained by other experiments.

1. Introduction

In the field of material science, there are two materials that have held a special position and have attracted significant attention due to a variety of their physical properties and a prospect of numerous applications. These are the wide bandgap semiconductor – zinc oxide (ZnO) and the ceramic material – aluminum oxide (Al_2O_3).

Most often, ZnO crystallizes as a hexagonal wurtzite structure with the direct band gap of 3.4 eV and the crystal-growth direction along the *c* axis. These properties qualify ZnO as a material suitable for application in the optoelectronic devices. In addition, a unique optical, acoustic and electric properties of ZnO, such as the high binding energy of 60 meV, high radiation, as well as chemical and thermal resistance, can be useful in the light-emitting UV and laser diodes, solar cells, gas sensors, biosensors, varistors, and surface acoustic wave devices [1,2].

Due to different positions of aluminum ions in the oxygen sublattice, aluminum oxide can exist in a variety of metastable structures as well as in its stable α-Al_2O_3 phase, which makes it suitable for many different uses and consequently results in the high production of aluminum oxide worldwide. For example, it is applied in the chemical industry as an adsorbent, abrasive, filler, ceramics, refractory, and catalyst; it is used as the protective barrier against corrosion, alternative surgical material for implants, as well as in the fabrication of the cutting tools and electronic devices [3,4].

In addtion to the important features of ZnO and Al_2O_3 themselves, materials that combine the two have been proven to have properties of good candidates for a wide range of applications. For example, spinel $ZnAl_2O_4$ may be applied in photoelectronic devices, optical coatings, stress imaging devices, and electroluminesence displays due to its wide energy bandgap, high values of fluorescence efficiency, photocatalytic activity, mechanical resistance, chemical and thermal stability, as well as low surface acidity [5–7]. In a number of studies it has been shown that the optical properties of spinel $ZnAl_2O_4$ depend strongly on the method used to prepare the material and the achieved morphology of the material [8–12]; namely, nanodimensional structures introduced enhanced optical and fluorescence properties that were not present in the bulk material. Further, the optical and fluorescence properties depend on the particle size that was achieved, as well. This is expected since larger specific surface area of smaller particles and consequent more present dangling and unsaturated bonds on the particle surface

* Corresponding author.
E-mail address: branka@ipb.ac.rs (B. Hadzic).

https://doi.org/10.1016/j.jlumin.2020.117273
Received 26 September 2019; Received in revised form 17 March 2020; Accepted 2 April 2020
Available online 8 April 2020

affect defect levels and material properties [13]. Methods of spinal $ZnAl_2O_4$ synthesis vary from the hydrothermal [11], solvothermal [14], microwave-hydrothermal [15], co-precipitation [10], sol-gel [16], combustion synthesis [17], citrate precursor [8], polymeric precursor [18], solid-state reaction method [19,20] to self-generated template [19]. The main disadvantage of the co-precipitation, solid-state reaction, and other common synthesis methods is the large obtained particle size.

With the aim to obtain small diameter nanoparticles of $ZnAl_2O_4$ surrounded by ZnO we used the calcination and hydrothermal method.

The luminescence was used as the principal method of investigation, whereas the XRD, Raman spectroscopy, and IR spectroscopy in the MID range [1–20] where used to characterize the samples. The elipsometric spectroscopy was employed as an aid in the analysis [21]. In addition to the standard methods of characterization of this group of materials, we used the IR spectroscopy in the far-infrared region to detect electron-phonon interaction, which further led to the explanation of the luminescence spectra.

The infrared (IR) spectroscopy is a well-known, simple, and reliable technique that is widely used in studying inorganic and organic materials. It is the absorbing type of spectroscopy, namely, different components of investigated materials absorb infrared light in a different wavelength domain. Consequently, the IR spectroscopy is very sensitive in detecting the presence of functional groups as well as of a single molecule type within a sample, since they each have a different characteristic spectrum that is often referred to as the fingerprint. The main advantages of the IR spectroscopy are the high scan speed, high resolution, high sensitivity, and wide range of application; it does not destroy the sample, and it provides a large amount of information. These advantages of the IR spectroscopy are followed by its use not only as a method for material analysis in science but in the industry as well. For example, it is used in the quality control, dynamic measurements, forensic analysis, identification and analysis of art pieces in general as well as of pigments in paintings, polymer manufacture, semiconductor microelectronics, food industry, gas leak detection devices, etc. [22–27]. In our study, it was the method of choice because it provides insight into the plasmon – phonon interaction. Recorded phonons participate in electron transfers and they must be included in the photoluminescence spectra analysis.

The interaction of electrons with crystal lattice vibrations denoted as phonons plays a significant role in shaping various properties of materials, for example, electrical characteristics of semiconductor-based devices, superconductivity, and the existence of the charge-density waves. Coupling of the longitudinal optical (LO) phonons with the surrounding free charge carrier plasmons result in the formation of the combined LO phonon – plasmon modes (CPPM). The published research most often investigate the interaction between a single phonon and effective plasmons in the n-type semiconductors, as well as the consecutive influence of the plasmon damping on the CPPM [28].

We intend to combine the Raman, far-infrared and photoluminescence spectroscopy to study the fundamental properties of combined plasmon – phonon modes in the ZnO–Al_2O_3 nanoparticles as well as the influence of sample preparation method and dopant concentration on the characteristics of obtained materials.

2. Samples preparation and characterization

The nanocrystalline samples of ZnO doped with Al_2O_3 were obtained by two methods. In the first method, the co-precipitation/calcination method, a mixture of aluminum and zinc hydroxides was obtained by adding an ammonia solution to a 20% solution of a proper amount of Zn $(NO_3)_2$*$6H_2O$ and $Al(NO_3)_3$*$4H_2O$ in water. The obtained hydroxides were filtered, dried, and calcinated at 300 °C for 1 h. The co-precipitation/calcination method is further referred to as the calcination method.

In the second method, namely, in the hydrothermal synthesis, a similar procedure was applied. Instead of the ammonia solution, now the 2 M solution of KOH was used. The obtained hydroxides were then put in a reactor with the microwave emission. The microwave assisted synthesis was conducted under the pressure of 3.8 MPa that was applied for 30 min. The synthesized product was filtered and dried. The hydrothermal synthesis is further denoted as the hydrothermal method. Each of the described two methods were used to obtain series of nano-sized $(ZnO)_{1-x}(Al2O3)_x$ samples with the nominal concentration of Al_2O_3 ranging from $x = 0$ to 0.7.

Powders obtained by chemical methods were pressed under very small preassure into tablets with 1 cm in diameter. The tablets were used in the vibrational measurements.

2.1. X-ray spectroscopy

The powder diffraction technique (XRD), was applied to determine the phase composition of the samples, using the X'Pert Philips device with the CoK_α radiation, in the 2θ mode. The detail phase composition study revealed the presence of crystalline phases of the hexagonal ZnO and spinel structured $ZnAl_2O_4$ in the samples synthesized by both methods, namely, by the co-precipitation/calcination as well as by the hydrothermal method (Fig. 1).

The XRD data was combined with the Scherrer's formula to determine the mean crystallite size in the studied samples [29]. To determine the mean crystallite size of ZnO phase, the diffraction peak corresponding to (102) reflection (at about $2\theta = 47°$) was taken, and to determine the mean crystallite size of the spinel $ZnAl_2O_4$ phase - a diffraction peak corresponding to the (400) reflection (located at about $2\theta = 44°$) was taken, respectively. It was found that the mean crystallite size, *d*, varies between 12 and 81 nm for the ZnO phases and is of the order of 5 nm for the $ZnAl_2O_4$ phases in the samples obtained by the calcination method, whereas for the samples that were obtained by the hydrothermal method the mean crystallite sizes were determined to be between 22 and 100 nm for the ZnO phases and from 5 to 13 nm for the $ZnAl_2O_4$ phases. The results of the XRD measurements, i.e., the phase compositions, as well as the mean crystallite size, are summarized in Table 1.

The results given in Table 1 indicate that, regardless of the method used to prepare the samples, the crystallite size of ZnO does not change monotonously with the increase of Al_2O_3 concentration. An increase of the ZnO crystallinity above the Al_2O_3 concentration of 20 wt% can be explained by faster transformation of smaller ZnO particles into spinel phase. As smaller particles of ZnO are more prone to react with Al_2O_3 to form a spinel, then the larger ZnO particles remain in the system as non-reacted, giving in the result an increased mean particle size of ZnO phase.

The crystallite size of the phase $ZnAl_2O_4$ in the samples obtained by the calcination method is constant, whereas, for the samples obtained hydrothermally, it becomes constant after the initial decrease with the increase of Al_2O_3 concentration. Consequently, the change of crystallite size of $ZnAl_2O_4$ with the nominal content of Al_2O_3 is smaller than for the ZnO phase. For both methods the obtained data didn't allow to obtain the size of ZnO crystallites above 50% of nominal content of Al_2O_3 although their presence has been registered in Fig. 1.

Similarly, for the samples with low Al_2O_3 concentration (up to 30% of Al_2O_3 for calcination method, and up to 10% of Al_2O_3 for hydrothermal method) the presence of the $ZnAl_2O_4$ phase has been registered; however the data didn't allow to calculate the size of nanocrystallites. Note that the crystallite size of the $ZnAl_2O_4$ phase in the samples obtained by both methods is constant for dopant concentrations higher than 50% (a stoichiometric concentration of Al_2O_3 in the spinel as about 55 wt%). For the highest dopant concentration of 70%, the XRD spectrum corresponding to the hydrothermally prepared sample reveals existence of the AlOOH phase (Fig. 1), as there is an excess of aluminum in the system, and not enough ZnO to form the spinel. The size of ZnO crystallites in the samples obtained by the hydrothermal method is

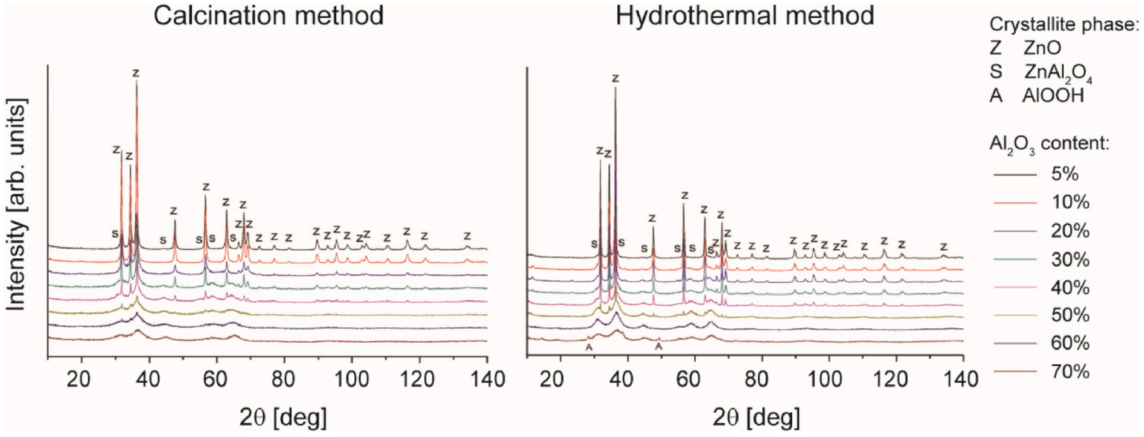

Fig. 1. XRD spectra of $(ZnO)_{1-x}(Al2O3)_x$ nanoparticles. The spectra are grouped into graphs according to the method used to prepare the samples, namely the calcination and hydrothermal method. The spectra given for the eight values of the dopant content, *x*, are differentiated by the line color. Three different crystallite phases were detected, Z, S, and A, which correspond to the ZnO, $ZnAl_2O_4$, and AlOOH, respectively.

Table 1
Mean crystallite size. The Scherrer's formula and XRD measurements were used to identify crystalline phases and calculate the mean crystallite size, *d*. The obtained results illustrate the dependence of mean crystallite size on the Al_2O_3 presence as well as on the method used to prepare the samples (calcination and hydrothermal method).

Al_2O_3 wt.%	*d* [nm] ZnO phase calcination	*d* [nm] ZnO phase hydrothermal	*d* [nm] $ZnAl_2O_4$ phase calcination	*d* [nm] $ZnAl_2O_4$ phase hydrothermal
5	25	41	–	–
10	26	22	–	–
20	12	50	–	13
30	31	34	–	7
40	81	100	5	5
50	–	–	5	5
60	–	–	5	5
70	–	–	5	5

larger than in the samples obtained by the calcination method. A reverse relationship was observed in our previous studies of the nanosized ZnO samples doped with other metal oxides [30–32]. The observed dependence is probably caused by the extension of the hydrothermal synthesis time to 30 min compared to the 15 min long synthesis that was used in our previous studies. Longer synthesis time caused ZnO crystallites to undergo significant agglomeration. Note that no other crystal phases besides the reported ones were observed in all the examined samples.

2.2. Scanning electron microscope (SEM)

The morphology of samples was investigated using the scanning electron microscope LEO 1530. The SEM images of the four representative samples for the calcination as well as hydrothermal method of sample preparation are given in Fig. 2.

The SEM characterization revealed a broad diversity in the morphology of samples. The images of samples with 10%, 30%, 50%, and 70% of Al_2O_3 are shown in Fig. 2. For the calcinated samples two types of agglomerates were observed: the plate-like agglomerates bigger than 100 nm and the smaller, spherical ones. It can be assumed that the larger and smaller ones correspond to the ZnO and $ZnAl_2O_4$ phase, respectively. In the calcinated samples with 50% of Al_2O_3 the particles that belong to the ZnO phase are covered with the smaller $ZnAl_2O_4$ particles, whereas for the Al_2O_3 concentration of 70%, the small particles that belong to the $ZnAl_2O_4$ phase dominate.

In the SEM images of the samples obtained by the hydrothermal method, the hexagonal agglomerates are observed for the sample with 30% of Al_2O_3 in addition to the previously discussed morphologies. In the sample with the Al_2O_3 concentration of 70% the homogeneous agglomerates that can be related to the $ZnAl_2O_4$ phase are visible.

For both methods of synthesis, the smallest agglomeration is observed in the samples with a high nominal content of the aluminum oxide. Note that these results agree well with those that were obtained by the XRD measurements.

3. Vibrational spectroscopy

The phases of ZnO and $ZnAl_2O_4$ were previously registered by the XRD measurements. Since the understanding of vibrational properties of the bulk material is crucial for the analysis of the vibration properties of nanoparticles, we begin the analysis of vibrational properties with a brief report of the literature data of the registered phases. The bulk modes are expected to be shifted and broadened as a consequence of the miniaturization.

The zinc oxide crystallizes in the wurtzite type hexagonal structure, and the growth of its crystals occurs along the *c*-axis [33]. Since the unit cell of zinc oxide contains four atoms, its spectrum is characterized by twelve vibrational modes: the three acoustic modes (one longitudinal and two transverse) and nine optical modes. The dispersion of optical phonons at the Γ point of the Brillouin zone is represented by the optical modes $2E_2 + 2E_1 + 2A_1 + 2B_1$. The modes E_1, E_2, and A_1 are active in the Raman scattering. The modes E_1 and A_1 are active in the infrared spectroscopy, and the modes B_1 are the "silent modes". The optical modes E_1 and A_1 are split at the Γ point into the transverse and longitudinal modes by the macroscopic crystal field. The splitting of the E_1 and A_1 modes is caused by the anisotropy of the ZnO crystal. In particular, the A_1 vibrations are parallel to the crystallographic *c*-axis, whereas the E_1 vibrations are perpendicular to it. Two sets of parameters are required to describe the dielectric function of a phonon, i.e., $\varepsilon_{xx} = \varepsilon_{yy} \equiv \varepsilon_{\perp}$ and $\varepsilon_{zz} \equiv \varepsilon_{||}$, along the electric field vector ($\boldsymbol{E}$), perpendicular ($\boldsymbol{E} \perp c$), and parallel ($\boldsymbol{E} \,||\, c$) to the crystal *c*-axis, respectively [34].

The Zn-aluminate, $ZnAl_2O_4$, crystallizes in the space group Fd3m with two formula units in the primitive rhombohedral unit cell [35]. The Zn and Al occupy the tetrahedral and the octahedral positions, respectively, in the close cubic oxygen packing. The group-theory analysis shows that 39 zone-center optical phonons are classified by the following symmetries [36]: the $\Gamma = A_{1g} + 2A_{2u} + E_g + 2E_u + T_{1g} + 4T_{1u} + 2T_{2u} + 3T_{2g}$. All the E modes are double degenerate, and all the T modes are ternary degenerate. The A_{1g}, E_g, and all the T_{2g} modes are Raman active, while all the T_{1u} modes are infrared active.

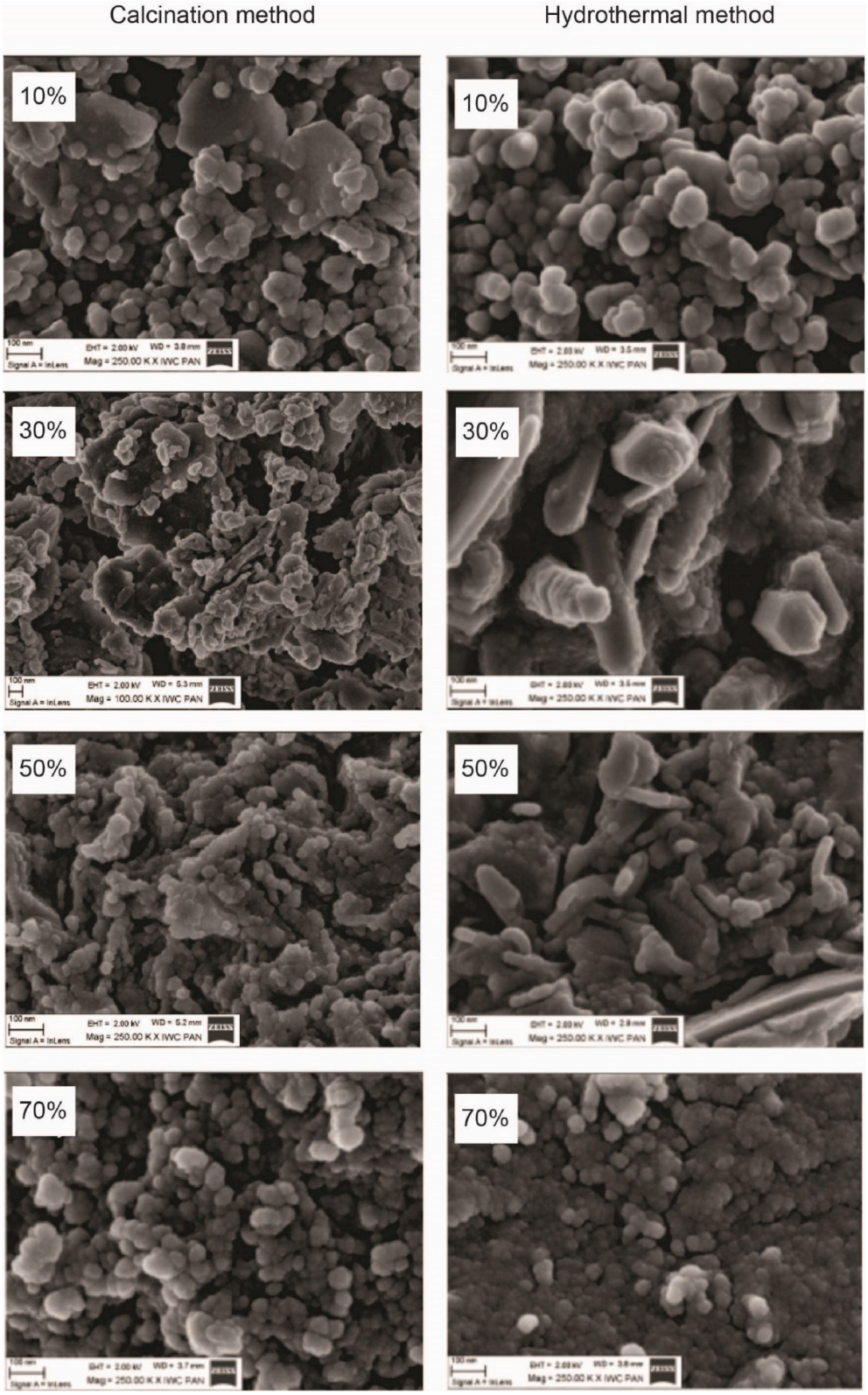

Fig. 2. SEM images of $(ZnO)_{1-x}(Al2O3)_x$ nanoparticles. The images of the samples with the Al_2O_3 content, *x*, of 10, 30, 50, and 70% that were prepared by the calcination as well as by the hydrothermal method, are given.

3.1. Raman spectroscopy

The micro-Raman spectra were taken in the backscattering configuration and analyzed using Jobin Yvon T64000 spectrometer, equipped with nitrogen cooled charge-coupled-device detector. As an excitation source we used the Verdi G optically pumped semiconductor laser with the 532 nm line. The measurements were performed at 60 mW laser power, which is the same power density as was the case for the photoluminescence measurements.

In Fig. 3 four representative spectra for samples prepared by the both

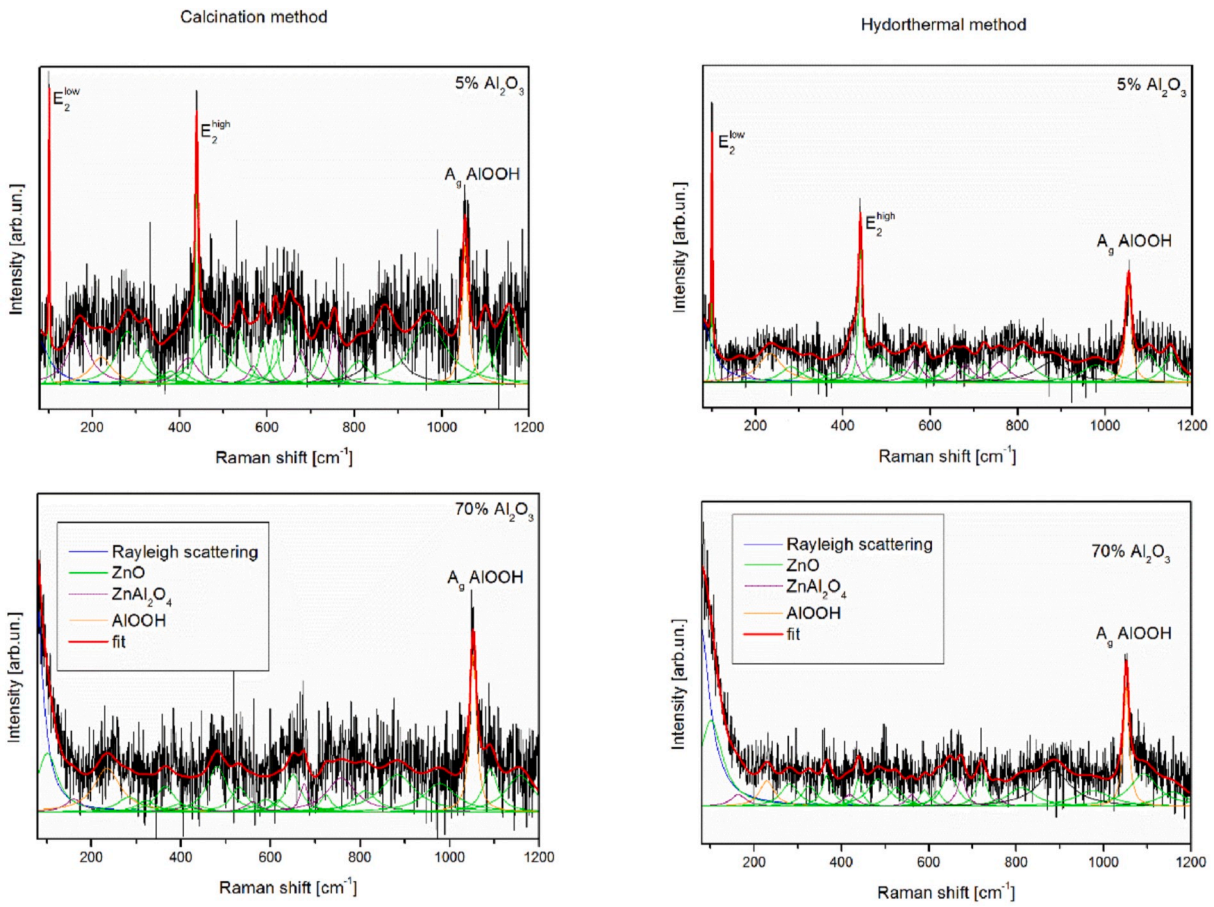

Fig. 3. Raman spectra of $(ZnO)_{1-x}(Al2O3)_x$ nanoparticles. The spectra are given for the reprezentative samples prepared by the calcination as well as by the hydrothermal method. The measured spectra are represented by dark line, theoretical spectra is depicted by a thick line, and the components that comprise the approximated curve are given as thin lines Eq. (1). The parameter defining different curves is the percentage of Al_2O_3.

methods and with nominal dopant concentration of 5% and 70% Al_2O_3 are shown. The Raman spectra are often analyzed using the convolution of the Lorentzian functions, each of which has line intensity, I, given with

$$I(\omega) = \frac{2A}{\pi} \frac{W}{4(\omega - \omega_c)^2 + W^2}, \quad (1)$$

where ω_c, W, and A are the position of the maximum, the half-width of the peak, and peak intensity, respectively. The measured data depicted with lines in Fig. 3 are approximated with the calculated thick curve, which represents the sum of the components each defined with Eq. (1).

By using all Raman active peaks that correspond to $ZnAl_2O_4$, such as 169, 417, 566, 682 and 758 cm^{-1} [36], and most of the peaks related to ZnO, such as 101, 284, 333, 378, 410, 437, 483, 536, 590, 618, 657, 723, 812, 980, 1105 and 1158 cm^{-1} [30], it was possible to reproduce the obtained experimental spectra. For the smaller dopant concentration, for both types of samples the most dominant peaks in the spectra are the two well-known ZnO peaks at 101 (E_2^{low}) and 437 cm^{-1} (E_2^{high}). All four representative spectra characterize one more peak towering above others. The peak at 1053 cm^{-1} belongs to the AlOOH phase. ZnO has multi phonon peak at 1054 cm^{-1}; however, due to the shape and FWHM (full width at half maximum) of the obtained peak in all four experimental Raman spectra it can assumed that this peak belongs to AlOOH phase. The existence of this phase is also confirmed by another peak at 232 cm^{-1} that is present in all the obtained spectra [37]. Consequently, it can be concluded that when ZnO is doped with Al_2O_3 three phases are formed, namely, ZnO, $ZnAl_2O_4$, and AlOOH. Low visibility of the AlOOH phase in the XRD measurements lead to the conclusion that the concentration of AlOOH is low but it increases with the increase of the dopant (Al_2O_3) concentration, which once more confirms high sensitivity of the Raman spectroscopy.

Taking into account the results obtained with XRD as well as Raman measurements we get a clear picture of phases present in the investigated ZnO–Al_2O_3 nano-system.

3.2. Far-infrared spectroscopy

The far-infrared measurements were carried out with a BOMEM DA – 8 FIR spectrometer. A DTGS pyroelectric detector was used to cover the wavenumber range from 80 to 680 cm^{-1}. The far-infrared spectra at room temperature of ZnO–Al_2O_3 nanopowders obtained by the calcination and hydrothermal methods are presented in Fig. 4. The experimental data are presented by circles, whereas the solid lines are used to show the calculated spectra.

Let us consider the interaction between a visible light of wavelength λ and semiconducting nanoparticles that are defined by their characteristic size, d, and dielectric function, ε_2, and are distributed in a medium with the dielectric constant ε_1. If a heterogeneous composite can be treated as a homogeneous medium with the effective dielectric permittivity, ε_{eff}, and the condition that relates the light and the nanoparticles, $\lambda \gg d$, is satisfied than the effective medium theory can be applied in a study of the interaction. There are many mixing models of the effective dielectric permittivity that correspond to such a mixture [38]. Since our samples are well defined and separated nanosized grains (Fig. 2), we used the Maxwell-Garnet model. For the spherical inclusions, spheres of permittivity ε_2 are located randomly in a homogeneous environment with permittivity ε_1 and occupy a volume fraction f.

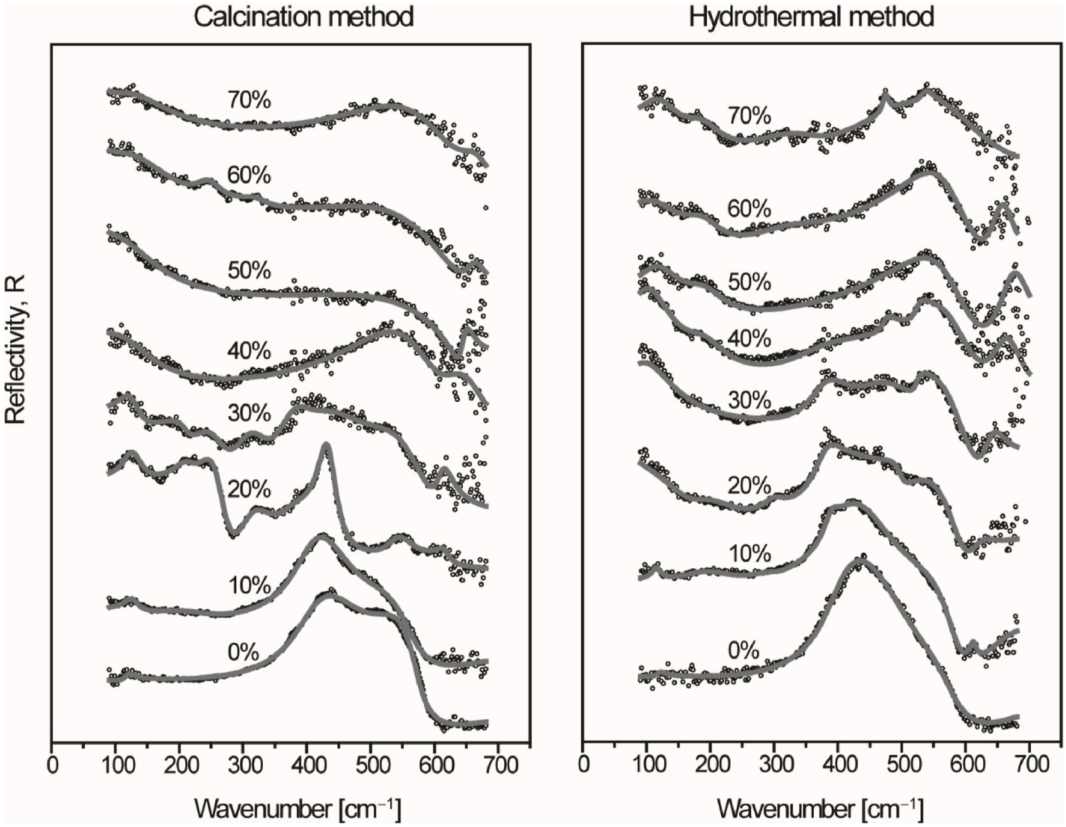

Fig. 4. Far-infrared reflection spectra of $(ZnO)_{1-x}(Al2O3)_x$ nanoparticles prepared by calcination and hydrothermal methods. The experimentally obtained data points are depicted by circles. The theoretical spectra given as the solid lines are obtained with the model defined by Eqs. (2) and (4) and the fitting procedure. The curve parameter is the dopant content, *x*, in percentages.

According to the Maxwell-Garnet mixing rule, the prediction of the effective permittivity of such a mixture is [39,40].

$$\varepsilon_{eff} = \varepsilon_1 + 3f\varepsilon_1 \frac{\varepsilon_2 - \varepsilon_1}{\varepsilon_2 + 2\varepsilon_1 - f(\varepsilon_2 - \varepsilon_1)}, \tag{2}$$

The ZnO–Al_2O_3 nanoparticles are situated in the air, therefore $\varepsilon_1 = 1$. Defining ε_2, the dielectric function of ZnO–Al_2O_3 nanoparticles is not so straight forward. The low-frequency dielectric properties of single crystals are described with the classical oscillators corresponding to the TO-modes, to which the Drude part is superimposed in order to take into account the free carrier contribution [41]. Consequently, the dielectric function of a single crystal takes the form

$$\varepsilon_s(\omega) = \varepsilon_\infty + \sum_{k=1}^{l} \frac{\varepsilon_\infty\left(\omega_{LOk}^2 - \omega_{TOk}^2\right)}{\omega_{TOk}^2 - \omega^2 - i\gamma_{TOk}\omega} - \frac{\varepsilon_\infty \omega_P^2}{\omega(\omega + i\Gamma_P)}, \tag{3}$$

where ε_∞ is the high frequency dielectric constant, ω_{LOk} and ω_{TOk} are the longitudinal and transverse optical phonon frequencies, ω_P is the plasma frequency, γ_{TOk} is the damping of host crystal modes, and Γ_P is the plasmon mode damping coefficient.

For the ZnO–Al_2O_3 nanoparticles, the pure LO modes of the lattice are strongly influenced by the plasmon mode, ω_P, which causes the appearance of a combined plasmon – LO phonon mode (CPPM) [41,42]. Consequently, if the LO mode is to be determined, the influence of free carriers must be eliminated. Hence, in the analysis of far-infrared reflection spectra of our samples, we used the dielectric function that includes the interaction between the LO phonon and a plasmon, i.e., the plasmon – phonon interaction [41,43].

$$\varepsilon_2(\omega) = \varepsilon_\infty \frac{\prod_{j=1}^{2}\left(\omega^2 + i\gamma_{lj}\omega - \omega_{lj}^2\right)}{\omega(\omega + i\Gamma_P)\left(\omega^2 + ig\omega - \omega_t^2\right)} \prod_{k=1}^{s} \frac{\omega^2 + i\gamma_{kLO} - \omega_{kLO}^2}{\omega^2 + i\gamma_{kTO} - \omega_{kTO}^2}. \tag{4}$$

The ω_{lj} and γ_{lj} (j = 1, 2) parameters of the first numerator are the eigenfrequencies and damping coefficients of the longitudinal plasmon – phonon (LP + LO) waves, that arise from the interaction of the initial modes (ω_{LO} corresponding to ZnO or ω_{LO} corresponding to Al_2O_3 (actually $ZnAl_2O_4$), and ω_P). The parameters of the first denominator correspond to the transverse (TO) vibrations. The second term represents the uncoupled modes of a crystal, where s is the number of uncoupled modes, ω_{LO} and ω_{TO} are the longitudinal and transverse frequencies, and γ_{LO} and γ_{TO} are the damping coefficients of the k-th crystal mode.

Therefore, the TO mode frequencies were obtained directly from the fit, whereas the LO modes were determined by the maximum of the dielectric loss function. As a result, the combined plasmon – LO phonon modes (ω_{l1}, ω_{l2}) were observed. In the experimental spectra, only the coupled-mode positions are observable. Therefore, detection of the LO-modes is closely related to the decoupling procedure [41]. The described procedure, i.e., the dielectric function from Eq. (2) and ε_2 from Eq. (4) is used to obtain the curves depicted with solid lines in Fig. 4.

The parameter adjusment was carried out automatically, using the least-square fitting of the theoretical (R_t) and experimental (R_e) reflectivity at q arbitrarily taken points:

$$\delta = \sqrt{\frac{1}{q}\sum_{j=1}^{q}\left(R_{ej} - R_{tj}\right)^2} \tag{5}$$

The value of δ was minimized until it complied with the commonly

accepted experimental error (less than 3%). For all the samples the determination errors of frequencies and damping coefficients were in the range 3–6 and 10–15%, respectively. The exact values of all determined phonon parameters are given in Tables S1 and S2 of the Supplementary material.

The dependence of the plasma frequency, ω_P, high-frequency dielectric constant, ε_∞, and filling factor, f, on the dopant content is given in Fig. 5. The plasma frequency is given as $\omega_P = \omega_{l1}\omega_{l2}/\omega_t$, ($\omega_P^2 \sim N$, where N is the free carriers concentration) [41]. Note that the dopant content of 20% acts as the limiting value that separates two sets of spectra shown in Fig. 4. It is the same dopant content value of 20% that corresponds to the minimal value of ω_P, and, consequently, the lowest concentration of free carriers, N, in the samples prepared by the calcination method, as shown in Fig. 5. This causes the plasmon – phonon interaction to be the weakest and, therefore, the detection of the primal phonons to be the most accurate for this particular composite. In the samples prepared by the hydrothermal method, ω_P monotonically increases with the increase of dopant concentration. In the samples with dopant concentration below the 20%, an interaction between the plasma and the ZnO phonon ($\omega_{TO} = 370$ cm^{-1}) occurs, whereas for the composites on the other side of the limiting value of 20% the interaction of plasma and $ZnAl_2O_4$ phonon ($\omega_{TO} = 543$ cm^{-1} $T_{1u}(2)$ symmetry) is registered. This argumentation is supported by the dependence of ε_∞ on the sample composition. Note that it is the effective value of ε_∞ that is being considered here. For the samples obtained by the calcination method ε_∞ has the value of 2.6 for the pure ZnO, it decreases to the value of 1.3 for the samples with 20% of Al_2O_3, and then increases to reach the value of 8.3 for the Al_2O_3 content of 70% (Fig. 5).

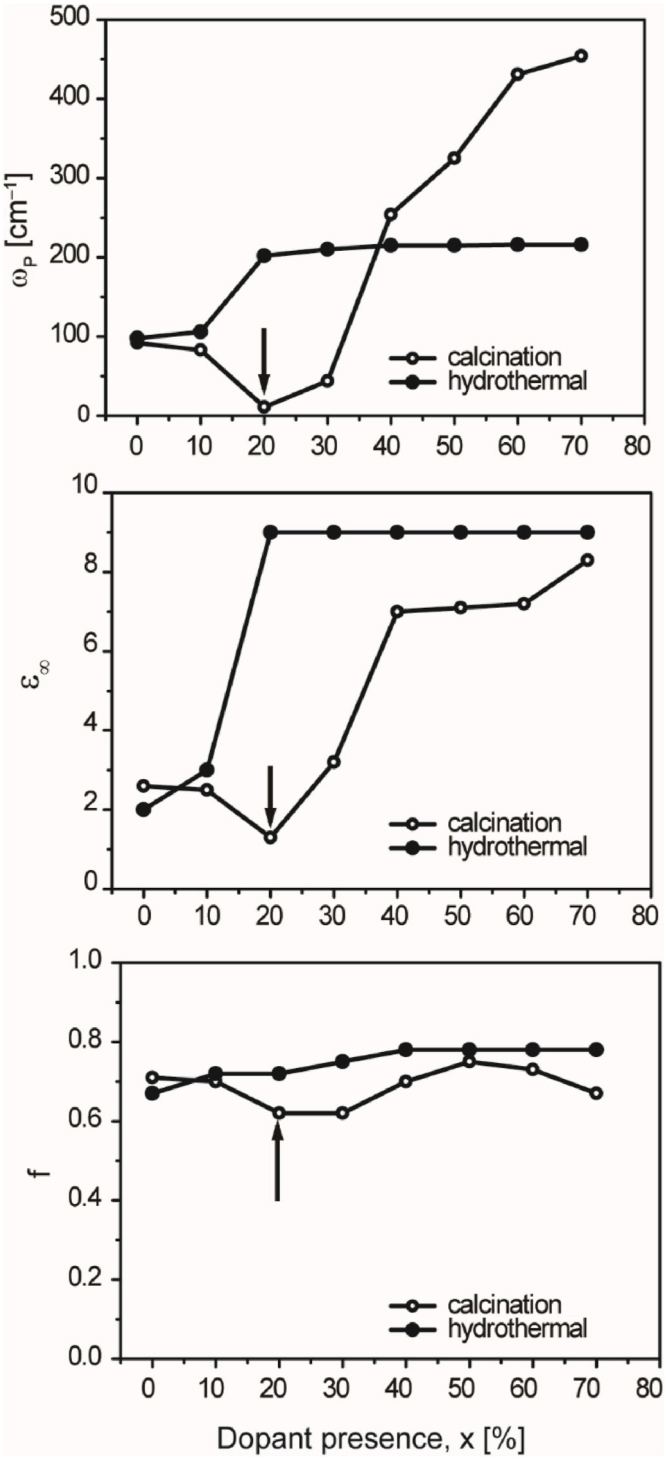

Fig. 5. Dependence of plasma frequency, ω_P, high frequency dielectric constant, ε_∞, and filling factor, f, on dopant content, x.

For the samples prepared by the hydrothermal method the ε_∞ dependence is different, namely, it increases monotonically with the dopant concentration increase. For all our samples the error in determining ε_∞ was 3%. The reflectivity measurements in the mid-infrared region that were used in this process are given in the Supplementary materials as Fig. S1Fig. S1. The filing factor, f, has a similar behavior, which is shown in Fig. 5 as well.

Characteristic spectra for the plasmon – LO phonon interaction are presented in Fig. 6. The frequencies of coupled modes (ω_{l1} and ω_{l2}) and the transverse mode frequencies marked by circles were obtained as the best fits. The lines labeled as ω_+ and ω_- are the solutions of the real part of Eq. (3), namely of $\mathrm{Re}\{\varepsilon_S\} = 0$. The values of the LO and TO frequencies that correspond to the ZnO and $ZnAl_2O_4$ are emphasized with the horizontal solid and dashed lines, respectively, for better visualization. As stated earlier, for the composites with 0% and 10% of Al_2O_3, a plasmon interacts with the ZnO phonon, whereas for the composites with the Al_2O_3 content larger than 20%, the interaction of a plasmon with the $T_{1u}(2)$ $ZnAl_2O_4$ phonon occurs. From the results given in Fig. 6 it is evident that the plasmon – phonon interaction exists in the entire range of the studied composites. Note that the experimental and the theoretical spectra match perfectly well.

To obtain a good match between the experimental and the theoretical spectra are given in Fig. 4, several phonons that were not predicted by the selection rules, had to be taken into account in the analysis of certain composites. The TO-LO splitting registered in some phonons is a result of the plasmon-phonon interaction, as can be seen in Tables S1 and S2. The phonon at approximately 110 cm^{-1}, that is most commonly attributed to a defect mode [44] was included in the spectral interpretation of all studied samples. As was the case in the Raman spectra, the phonons at 320, 378, 426, 483, 536, 600, and 670 cm^{-1} correspond to ZnO, whereas those around 200, 410, and 510 cm^{-1} are due to $ZnAl_2O_4$. Their appearance is caused by the attenuation of selection rules due to miniaturization. This effect might be the main reason for the difference between the phonons resulting from the fitting procedure illustrated in Fig. 4 and those discussed in Ref. [45]. On the other hand, a similar effect can be caused by the surface-optical phonons [30]; however, they are a consequence of nanoparticles formation, as well. Besides, in the spectra of the some samples the existence of weak modes at approximately 240 and 440 cm^{-1} that can be associated with the AlOOH phase, is evident. This is consistent with the results obtained by the XRD and Raman measurements that detected the AlOOH phase.

4. Photoluminescence spectroscopy

Optical properties of the samples were investigated with the photoluminescence (PL) spectroscopy. The spectro-fluometer SOLAR CM 2203 with the excitation wavelength of 300 nm (4.13 eV) was used and the obtained PL spectra are shown in Fig. 7. The measured spectra are

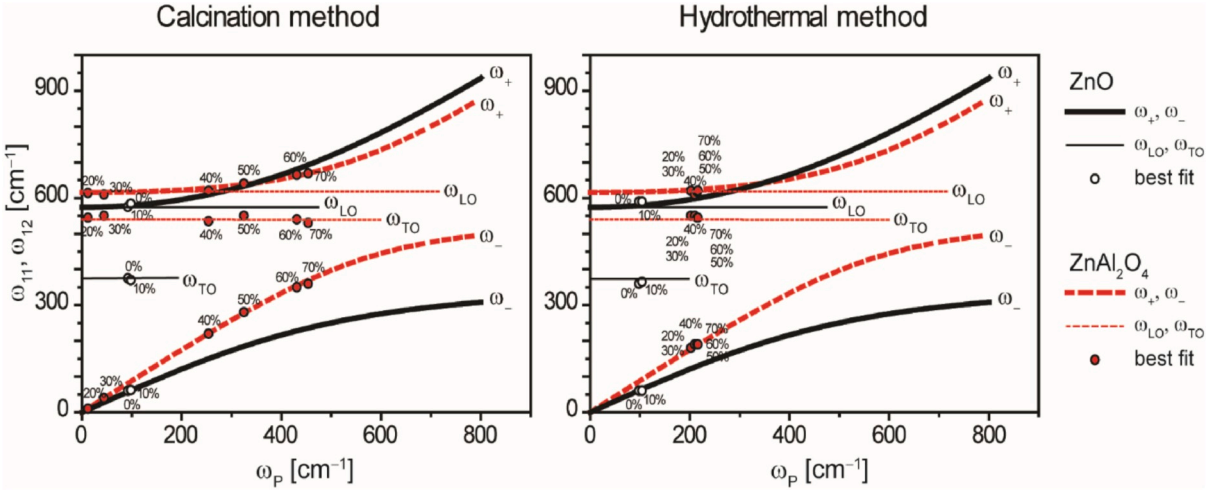

Fig. 6. Eigenfrequencies of plasmon-phonon modes of $(ZnO)_{1-x}(Al2O3)_x$ nanoparticles. The solid and dashed lines are the spectra calculated from $Re\{\varepsilon_s\} = 0$, where ε_s is given by Eq. (3), whereas the open and solid circles represent ω_{l1} and ω_{l2}. The black solid lines and open circles denote the coupling with the ZnO phonon, whereas the red, dashed lines and solid circles correspond to the coupling with the $ZnAl_2O_4$ phonon.

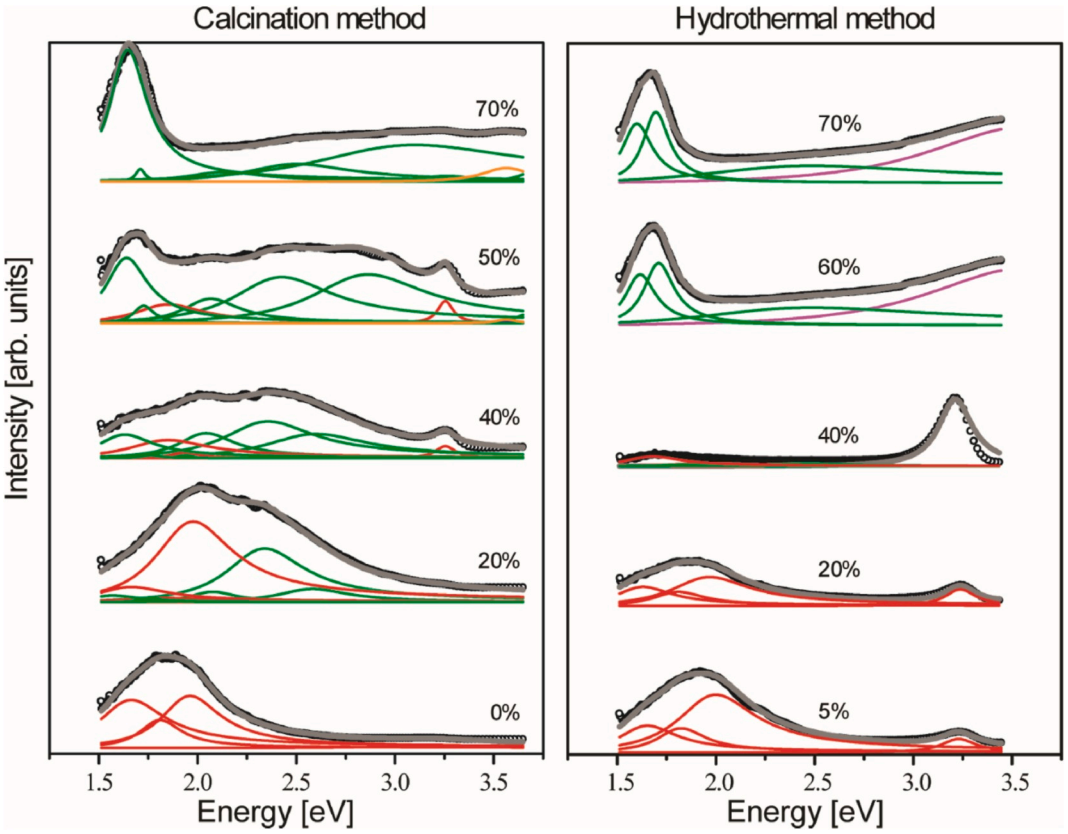

Fig. 7. Photoluminescence spectra of $(ZnO)_{1-x}(Al2O3)_x$ nanoparticles. The spectra are given for the samples prepared by the calcination as well as by the hydrothermal method. The measured spectra are represented by circles, theoretical spctra is depicted by a thick line, and the components that comprise the approximated curve are given as thin lines. The parameter defining different curves is the percentage of Al_2O_3.

represented by circles, and theoretical spectra is depicted by a thick line, and the components that comprise the approximated curve are given as thin lines (eq. (1)). The values of the positions, ω_c, and intensities, A, of the Lorentzian peaks that provide the best match between the experimental and theoretical spectra are given in Fig. 8.

The spectra in Fig. 7 that correspond to the samples obtained by the hydrothermal method can be divided: the spectra of samples with Al_2O_3 concentration below and above 40%. If the dopant concentration is lower and equal 40% the PL spectra contain two emission bands, namely the band at 3.20 eV and the broad structure centered at approximately 1.9 eV. For the composites with the dopant concentration higher than 40%, the emission band at 3.20 eV becomes wider and a new band appears at approximately 3.59 eV (purple).

The PL spectra of the samples prepared by the calcination method are qualitatively different from those corresponding to the hydrothermal method. If the samples were prepared by the calcination method,

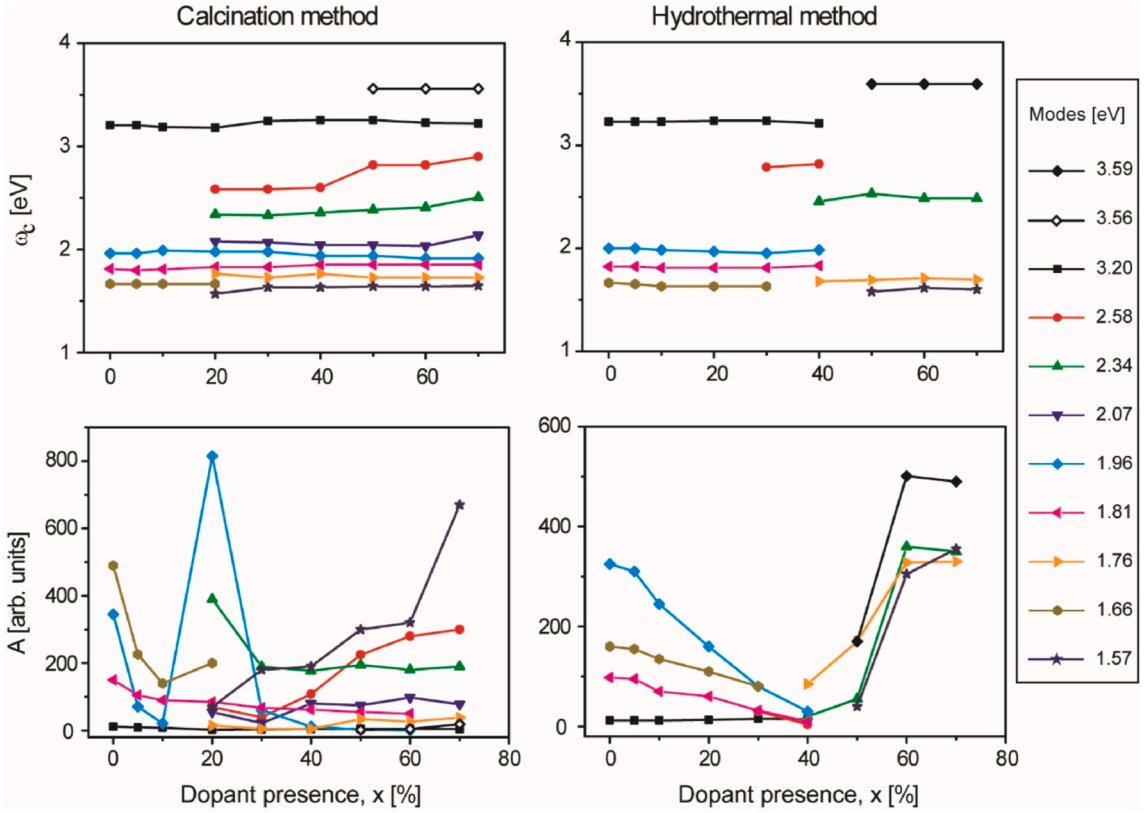

Fig. 8. Dependence of position and intensity of photoluminescence peaks on dopant concentration. For the nanoparticle compositions of $(ZnO)_{1-x}(Al2O3)_x$ prepared by the calcination as well as by the hydrothermal method, the dependence of the position, ω_c, and intensity, A, of the photoluminescence peaks on the dopant, Al_2O_3, presence, x, is given.

interweaving of all the bands occurs for almost all values of the dopant concentration in the composite. In this case, very weak emission was recorded around 3.56 eV for the samples with more than 40% of Al_2O_3 (orange).

For the hydrothermal method, the intensity of the peaks at 3.20, 2.58, 1.96, 1.81, and 1.66 eV decreases with the increase of the Al_2O_3 concentration in ZnO from 0 to 40% (Fig. 8). This indicates that these bands originate from ZnO; in Fig. 7 these Lorentzians are represented with the thin red lines. On the other hand, the bands at 2.34, 1.76, and 1.57 eV appear for the dopant content of 40% and more, and their intensity increases with the increase of dopant content; these $ZnAl_2O_4$ bands are represented in Fig. 7 with the thin green lines. Besade that, the peak located around 3.59 eV must be considered in the spectra corresponding to the samples with Al_2O_3 concentration larger than 40%. Taking into account the results obtained by the XRD, Raman, and IR measurements, it can be concluded that the emission in question is related to AlOOH, which is detected in our samples. Namely, the results presented in Ref. [46] indicate possible exsisance of a very broad emission in the range between 3 eV and 4 eV in AlOOH. In our case, this emission is supported by the presence of a metal Zn, which is used in disigning biosensors with this base [47]. Such wide emission masks the emission at 3.2 eV related to ZnO as can be seen in Fig. 7.

The structure of PL spectra that corresponds to the samples obtained by the calcination method is more complex. The peak positions are very close to those registered for the samples synthesized by the hydrothermal method. However, the bands that originate from the ZnO phase were registered independently only for the samples with the Al_2O_3 content of 10% or less. In all spectra with dopant content larger than 10% the bands corresponding to the $ZnAl_2O_4$ phase are present. The PL spectrum of the sample, with 20% of Al_2O_3 has several exciting features. The intensity of peaks at 2.34, 1.96, and 1.66 eV significantly deviates from the monotonous change, namely these peaks are much stronger for this particular value than for any other value of the dopant presence. Consequently, in addition to the enhanced intensity of these bands, the spectrum itself is more intense. Note that this peculiarity was discovered in various ways in the analysis of the infrared spectra as well. The UV band centered at about 3.20 eV originates from the near-band-edge exciton and bound exciton emission of ZnO crystallite. For the samples with more than 40% of Al_2O_3 a very weak, relatively narrow emission is noticed at 3.56 eV. Its intensity very slowly increases with the increase of Al_2O_3 presence in the sample. However, for samples obtained by the hydrothermal method, intensity of emission in that region is 20 times larger than was the case for the samples obtained by the calcination method. The emission is possitioned above the E_g of ZnO. In this case, the quantum confinement influence cannot be as strong as to move near-band-edge emission in ZnO to 3.6 eV, since nanoparticles smaller than 1 nm would be required. On the other hand, the value of E_g corresponding to $ZnAl_2O_4$ is arround 3.8 eV. In $ZnAl_2O_4$ narrow phonon supported emissions related to transfers from this level were reported [48]. Probably, one of the phonons of $T_{2g}(3)$, $T_{1u}(4)$, or $T_{2u}(2)$ symmetry in $ZnAl_2O_4$ that were detected in our Raman and IR measurements, participates in this emission, since their energies are appropriate. A detailed analysis is given in Ref. [48]. On the other hand, this emission can be related to the doping level formation in the range between the energy gaps of ZnO and $ZnAl_2O_4$ as suggested in Ref. [49].

On the other hand, for both methods, the bands at 2.58, 1.96, 1.81, and 1.66 eV are correlated with the radiative recombination of a photogenerated hole with an electron occupying the oxygen vacancy in ZnO [50–53], surface states [52,54], and interstitial oxygen defects, impurities as well as defects related to excess oxygen [55,56]. The bands at 2.34, 1.76, and 1.57 eV, which are related to the $ZnAl_2O_4$ phase, originate from the intra band gap defects, for example, oxygen vacancies, as suggested by Ragupathi et al. [57], Wang et al. [58] and Sun et al. [59].

5. Conclusions

The phase composition of nanocrystalline samples of ZnO–Al_2O_3 prepared by the co-precipitation/calcination method and by the hydrothermal synthesis was determined by the X-ray diffraction. The morphology was studied using SEM measurements. In all the studied samples, prepared by use of two different wet chemical methods, the crystalline phases of ZnO, $ZnAl_2O_4$ and AlOOH were identified. In our previous papers, we showed that physical properties (e.g., structural, magnetic) strongly depend on the synthesis method and conditions [60, 61].

The crystallite size of ZnO does not have a monotonous dependence on the nominal Al_2O_3 content. The crystallite size of the $ZnAl_2O_4$ phase is constant in the samples obtained by the calcination method, and it decreases with the increase of the Al_2O_3 content in the samples that were obtained by the hydrothermal method. The analysis of photoluminescence and far-infrared spectra of the samples prepared by the hydrothermal method indicated that the observed features as well as the electronic structure of the nanocomposites monotonically depend on nominal content of Al_2O_3. On the other hand, for the samples obtained by the calcination method with nominal Al_2O_3 content between 20 and 40% PL measurements revealed very complex spectra. In the analysis of the obtained far-infrared spectra, we treated our nanoparticles as homogenous spherical inclusions in air and modeled them by the Maxwell-Garnet formula. Besides the modes that are characteristic for the ZnO and $ZnAl_2O_4$ phases, the far-infrared spectroscopy detected the combined plasmon – LO phonon modes (CPPM). Taking the sample preparation method and dopant concentration as parameters, the relationship between the free carrier concentration and optical parameters was observed. The photoluminescence spectra contain emissions related to the presence of ZnO, $ZnAl_2O_4$, and AlOOH in the nanomaterials, which is in agreement with the results of other experiments.

Declaration of competing interest

The author(s) declared no potential conflicts of interest with respect to the research, authorship, and/or publication of this article.

Acknowledgments

This work was supported under the Agreement of Scientific Collaboration between Polish Academy of Science and Serbian Academy of Sciences and Arts. The work in Serbia was supported by the Serbian Ministry of Education, Science and Technological Development through the Project 45003.

Appendix A. Supplementary data

Supplementary data to this article can be found online at https://doi.org/10.1016/j.jlumin.2020.117273.

References

[1] P. Ooi, S. Lee, S. Ng, Z. Hassan, H. Abu Hassan, Far infrared optical properties of bulk wurtzite zinc oxide semiconductor, J. Mater. Sci. Technol. 27 (2011) 465.
[2] P.A. Rodnyi, I.V. Khodyuk, Optical and luminescence properties of zinc oxide, Optic Spectrosc. 111 (2011) 776.
[3] A. Boumaza, L. Favaro, J. Ledion, G. Sattonnay, J.B. Brubach, P. Berthet, A. M. Huntz, P. Roy, R. Tetot, Transition alumina phases induced by heat treatment of boehmite: an X-ray diffraction and infrared spectroscopy study, J. Solid State Chem. 182 (2009) 1171.
[4] R. Rinaldi, U. Schuchardt, On the paradox of transition metal-free alumina-catalyzed epoxidation with aqueous hydrogen peroxide, J. Catal. 236 (2005) 335.
[5] X.L. Duan, D.R. Yuan, F.P. Yu, Cation distribution in Co-doped ZnAl2O4 nanoparticles studied by X-ray photoelectron spectroscopy and 27Al solid-state NMR spectroscopy, Inorg. Chem. 50 (2011) 5460–5467.
[6] R. Ianos, S. Borcănescu, R. Lazaău, Large surface area ZnAl2O4 powders prepared by a modified combustion technique, Chem. Eng. J. 240 (2014) 260–263.
[7] E.L. Foletto, et al., Synthesis of ZnAl2O4 nanoparticles by different routes and the effect of its pore size on the photocatalytic process, Microporous Mesoporous Mater. 163 (2012) 29–33.
[8] X.Y. Li, Z.R. Zhu, Q.D. Zhao, L.Z. Wang, Photocatalytic degradation of gaseous toluene over ZnAl2O4 prepared by different methods: a comparative study, J. Hazard Mater. 186 (2011) 208–2096.
[9] C. Peng, et al., Fabrication and luminescence properties of one-dimensional ZnAl2O4 and ZnAl2O4: a^{3+} (A = Cr, Eu, Tb) microfibers by electrospinning method, Mater. Res. Bull. 47 (2012) 3592–3599.
[10] B.C. Cheng, Z.Y. Ouyang, B.X. Tian, Y.H. Xiao, S.J. Lei, Porous ZnAl2O4 spinel nanorods: high sensitivity humidity sensors, Ceram. Int. 39 (2013) 7379–7386.
[11] Z.R. Zhu, et al., Photocatalytic performances and activities of ZnAl2O4 nanorods loaded with Ag towards toluene, Chem. Eng. J. 203 (2012) 43–51.
[12] Y. Yang, et al., Hierarchical three-dimensional ZnO and their shape-preserving transformation into hollow ZnAl2O4 nanostructures, Chem. Mater. 20 (2008) 3487–3494.
[13] Z.Q. Yu, C. Li, N. Zhang, Size dependence of the luminescence spectra of nanocrystal alumina, J. Lumin. 99 (2002) 29–34.
[14] G.L. Fan, J. Wang, F. Li, Synthesis of high-surface-area micro/mesoporous ZnAl2O4 catalyst support and application in selective hydrogenation of o-chloronitrobenzene, Catal. Commun. 15 (2011) 113–117.
[15] M. Zawadzki, W. Staszak, F.E. López-Suárez, M.J. Illán-Gómez, A. Bueno-López, Preparation, characterisation and catalytic performance for soot oxidation of copper-containing ZnAl2O4 spinels, Appl. Catal. Gen. 371 (2009) 92–98.
[16] X. Wei, D. Chen, Synthesis and characterization of nanosized zinc aluminate spinel by sol–gel technique, Mater. Lett. 60 (2006) 823–827.
[17] R. Ianos, R. Lazău, I. Lazău, C. Păcurariu, Chemical oxidation of residual carbon from ZnAl2O4 powders prepared by combustion synthesis, J. Eur. Ceram. Soc. 32 (2012) 1605–1611.
[18] L. Gama, et al., Synthesis and characterization of the NiAl2O4, CoAl2O4 and ZnAl2O4 spinels by the polymeric precursors method, J. Alloys Compd. 483 (2009) 453–455.
[19] L. Zou, F. Li, X. Xiang, D.G. Evans, X. Duan, Self-generated template pathway to high-surface-area zinc aluminate spinel with mesopore network from a single-source inorganic precursor, Chem. Mater. 18 (2006), 5852–585.
[20] N.J. Van der Laag, M.D. Snel, P.C.M.M. Magusin, G. De With, Structural, elastic, thermophysical and dielectric properties of zinc aluminate (ZnAl2O4), J. Eur. Ceram. Soc. 24 (2004) 2417–2424.
[21] Elipsometar.
[22] D.A. Skoog, F.J. Holler, S.R. Crouch, Principles of Instrumental Analysis, sixth ed., Thomson Higher Education, Belmont, CA, 2007.
[23] D.C. Harris, M.D. Bertolucci, Symmetry and Spectroscopy: an Introduction to Vibrational and Electronic Spectroscopy, Dover Publications, New York, 1989.
[24] P. Ricciardi, Unlocking the Secrets of Illuminated Manuscripts, Laboratory News, 2012. Retrieved. (Accessed 11 December 2015).
[25] W.S. Lau, Infrared Characterization for Microelectronics, World Scientific, 1999, ISBN 981-02-2352-8.
[26] A. Villar, E. Gorritxategi, E. Aranzabe, S. Fernandez, D. Otaduy, L.A. Fernandez, Low-cost visible–near infrared sensor for on-line monitoring of fat and fatty acids content during the manufacturing process of the milk, Food Chem. 135 (2012) 2756.
[27] J. Coates, A review of new small-scale technologies for near infrared measurements, June 18 (2014). www.americanpharmaceuticalreview.com.
[28] N. Romcevic, M. Romcevic, W.D. Dobrowolski, L. Kilanski, M. Petrovic, J. Trajic, B. Hadzic, Z. Lazarevic, M. Gilic, J.L. Ristic-Djurovic, N. Paunovic, A. Reszka, B. J. Kowalski, I.V. Fedorchenko, S.F. Marekin, Far-infrared spectroscopy of Zn1-xMnxGeAs2 single crystals: plasma damping influence on plasmon-phonon interaction, J. Alloys Compd. 649 (2015) 375.
[29] A.L. Patterson, The scherrer formula for X-ray particle size determination, Phys. Rev. 56 (1939) 978.
[30] B. Hadžić, N. Romčević, M. Romčević, I. Kuryliszyn-Kudelska, W. Dobrowolski, J. Trajić, D. Timotijević, U. Narkiewicz, D. Sibera, Surface optical phonons in ZnO (Co) nanoparticles: Raman study, J. Alloys Compd. 540 (2012) 49.
[31] B. Hadžić, N. Romčević, M. Romčević, I. Kuryliszyn-Kudelska, W. Dobrowolski, R. Wrobel, U. Narkiewicz, D. Sibera, Raman study of surface optical phonons in ZnO(Mn) nanoparticles, J. Alloys Compd. 585 (2014) 214.
[32] B. Hadžić, N. Romčević, M. Romčević, I. Kuryliszyn-Kudelska, W. Dobrowolski, U. Narkiewicz, D. Sibera, Influence of SOP modes on Raman spectra of ZnO(Fe) nanoparticles, Opt. Mater. 42 (2015) 118.
[33] V.S. Vinogradov, V.N. Dzhagan, T.N. Zavaritskaya, I.V. Kucherenko, N.N. Melnik, N.N. Novikova, E. Janik, T. Wojtowicz, O.S. Plyashechnik, D.R.T. Zahn, Optical phonons in the bulk and on the surface of ZnO and ZnTe/ZnO nanowires in Raman spectra, Phys. Solid State 54 (2012) 2083.
[34] G. Mirjalili, T.J. Parker, S.F. Shayesteh, M.M. Bulbul, S.R.P. Smith, T.S. Cheng, C. T. Foxon, Far-infrared and Raman analysis of phonons and phonon interface modes in GaN epilayers on GaAs and GaP substrates, Phys. Rev. B 57 (1998) 4656.
[35] N.W. Wyckoff, Crystal Structures, vol. 2, Intersciences, New York, 1962.
[36] M.M. Sinha, J.S. Kim, Analysis of vibrational modes and phonon density of states of aluminate spinels, J. Kor. Phys. Soc. 43 (2003) 237.
[37] A.B. Kiss, G. Keresztury, L. Farkas, Raman and i.r. spectra and structure of boehmite (γ-AlOOH). Evidence for the recently discarded $D2h^{17}$ space group, Spectrochim. Acta 36 (1980) 653.
[38] K. Karkkainen, A. Saviola, K. Nikoskinen, Analysis of a three-dimensional dielectric mixture with finite difference method, IEEE Trans. Geosci. Rem. Sens. 39 (2001) 1013.

[39] J.C.M. Garnett, Colours in metal glasses and in metallic films, Trans. R. Soc. CCIII (1904) 385.
[40] A. Saviola, I. Lindell, Polarizability modeling of heterogeneous media, in: A. Priou (Ed.), Dielectric Properties of Heterogeneous Materials, PIER 6 Progres in Electromagnetic Research, Elsevier, Amsterdam, The Netherlands, 1992, p. 101.
[41] J. Trajic, N. Romcevic, M. Romcevic, V.N. Nikiforov, Plasmon-phonon and plasmon-two different phonon interaction in Pb1-xMnxTe mixed crystals, Mater. Res. Bull. 42 (2007) 2192.
[42] T. Hamaguchi S. Shimomura Takaoka, K. Murase, Observation of the coupled plasmon- lo phonon mode energy in photo-excited Pb1-xSnxTe doped with indium impurities, Solid State Commun. 54 (1985) 99.
[43] A.A. Kukharskii, Plasmon – phonon coupling in GaAs, Solid State Commun. 8 (1970) 1275.
[44] H. Kepa, T. Giebultowicz, B. Buras, B. Lebech, K. Clausen, A neutron scattering study of lattice dynamics of HgTe and HgSe, Phys. Scripta 25 (1982) 807.
[45] P. Ooi, S. Lee, S. Ng, Z. Hassan, H.A. Hassan, Far infrared optical properties of bulk wurtzite zinc oxide semiconductor, J. Mater. Sci. Technol. 27 (2011) 465.
[46] J. Garcia-Guinea, J. Rubio, V. Correcher, F.J. Valle-Fuenter, Luninescence of α-Al2O3 and α-AlOOH natural mixtures, Radiat. Meas. 33 (2001) 653–658.
[47] B. Rezaei, Z. Hassani, Z. Shshshanaipour, A.A. Ensafi, G. Mohammadnezhad, Applictions of modified mesoporous boehmite (γ-AlOOH) with green synthesis carbon quantum dots for a fabrication biosensor to determine trace amounts of docorucin, Luminescence 33 (8) (2018) 1377–1386.
[48] S.-F. Wang, G.-Z. Sun, L.-M. Fang, L. Lei, X. Xiang, X.-T. Zu, A comparative study of ZnAl2O4 nanoparticles synthesized from different aluminium salt for use as fluorescence material, Sci. Rep. 5 (2015) 12894.
[49] S.V. Motloung, P. Kumari, L.F. Koao, T.E. Motaung, T.T. Hlastshwayo, M. J. Mochane, Effects of anneling time on the structure and optical properties of ZnAl2O4/ZnO prepared via citrate sol/gel process, Mater. Today Commun. 14 (2018) 294–301.
[50] G. Shan, M. Zhong, S. Wang, Y. Li, Y. Liu, The synthesis and optical properties of the heterostructured ZnO/Au nanocomposites, J. Colloid Interface Sci. 326 (2008) 392.
[51] P. Chand, A. Gaur, A. Kumar, Structural and optical properties of ZnO nanoparticles synthesized at different pH values, J. Alloys Compd. 539 (2012) 174.
[52] P.B. Taunk, R. Das, D.P. Bisen, R.k. Tamrakar, Structural characterization and photoluminescence properties of zinc oxide nano particles synthesized by chemical route method, J. Radiat. Res. Appl. Sci. 8 (2015) 433.
[53] Q. Hou, F. Meng, J. Sun, Electrical and optical properties of Al-doped ZnO and ZnAl2O4 films prepared by atomic layer deposition, Nanoscale Res. Lett. 8 (2013) 144.
[54] S.A. Studenikin, N. Golego, M. Cocivera, Fabrication of green and orange photoluminescent, undoped ZnO films using spray pyrolysis, J. Appl. Phys. 84 (1998) 2287.
[55] K.H. Tam, C.K. Cheung, Y.H. Leung, A.B. Djurisic, C.C. Ling, C.D. Beling, S. Fung, W.M. Kwok, W.K. Chan, D.L. Phillips, L. Ding, W.K. Ge, Defects in ZnO nanorods prepared by a hydrothermal method, J. Phys. Chem. B 110 (2006) 20865.
[56] L.E. Greene, M. Law, J. Goldberger, F. Kim, J.C. Johnson, Y. Zhang, R.J. Saykally, P. Yang, Low-temperature wafer-scale production of ZnO nanowire arrays, Angew. Chem. Int. Ed. 42 (2003) 3031.
[57] C. Ragupathi, J.J. Vijaya, A. Manikandan, L.J. Kennedy, Phytosynthesis of nanoscale ZnAl2O4 by using sesamum (Sesamum indicum L.) optical and catlytic properties, J. Nanosci. Nanotechnol. 13 (2013) 8298.
[58] S.-F. Wang, G.-Z. Sun, L.-M. Fang, L. Lei, X. Xiang, X.-T. Zu, A comparative study of ZnAl2O4 nanoparticles synthesized from different aluminum salts for use as fluorescence materials, Sci. Rep. 5 (2015) 12849.
[59] G. Sun, G. Sun, M. Zhong, S. Wang, X. Zu, X. Xiang, Coordination mechanism, characterization and photoluminescence properties of spinel ZnAl2O4 nanoparticles prepared by a modified polyacrylamide gel route, Russ. J. Phys. Chem. A 90 (2016) 691.
[60] I. Kuryliszyn-Kudelska, B. Hadžić, D. Sibera, M. Romčević, N. Romčević, U. Narkiewicz, W. Dobrowolski, Dynamic magnetic properties of ZnO nanocrystals incorporating Fe, J. Alloys Compd. 509 (2011) 3756.
[61] I. Kuryliszyn-Kudelska, W. Dobrowolski, M. Arciszewska, A. Małolepszy, L. Stobiński, R. Minikayev, „Adjusting the magnetic properties of ZrO2:Mn nanocrystals by changing hydrothermal synthesis conditions", Magnetochemistry 4 (2018) 28.